*metals*

MDPI

*Article*

# Two Fatigue Life Prediction Models Based on the Critical Plane Theory and Artificial Neural Networks

**Yantian Wang [1], Yuanying Qiu [1,*], Jing Li [1,*] and Jin Bai [2]**

[1] School of Mechatronic Engineering, Xidian University, No. 2 South Taibai Road, Xi'an 710071, China
[2] Xi'an Aerospace Propulsion Test Technology Institute, Xi'an 710100, China
* Correspondence: yyqiu@mail.xidian.edu.cn (Y.Q.); j_li@xidian.edu.cn (J.L.)

**Abstract:** Since a multiaxial loading environment may lead to the fatigue failure of structures, establishing a reliable fatigue model to predict the multiaxial fatigue lives of structures has always been a concern of engineers. This study proposes a new multiaxial fatigue theoretical model (WYT model) based on the critical plane theory, which takes the plane of the maximum shear strain amplitude as the critical plane and considers the effects of shear stress and normal stress on fatigue damage. Moreover, a backpropagation neural network (BPNN) model for multiaxial fatigue life prediction with the shear strain amplitude, normal strain amplitude, mean shear stress, and mean normal stress on the same critical plane as input parameters and fatigue life as the output variable is established. Finally, the WYT model and the BPNN model are compared with two existing multiaxial fatigue models to evaluate the life prediction effects of different models for S45C and 7075-T651 under constant-amplitude and variable-amplitude multiaxial loadings. The calculation results show that the WYT model is feasible, and the BPNN model is more accurate in predicting the fatigue lives of specimens than other multiaxial fatigue theoretical models.

**Keywords:** multiaxial fatigue; critical plane theory; fatigue life prediction; neural network; fatigue damage



**Citation:** Wang, Y.; Qiu, Y.; Li, J.; Bai, J. Two Fatigue Life Prediction Models Based on the Critical Plane Theory and Artificial Neural Networks. *Metals* **2024**, *14*, 938. https://doi.org/10.3390/met14080938

Academic Editor: Denis Benasciutti

Received: 16 July 2024
Revised: 13 August 2024
Accepted: 14 August 2024
Published: 16 August 2024



## 1. Introduction

In many fields of industry, such as automobiles, aircraft, and marine ships, engineering structures are often subjected to multiaxial loading and may experience fatigue failure during use [1,2]. Under complex loading paths, the multiaxial fatigue lives of structures are more difficult to predict [3,4]. For example, the attachments of a turbine blade to the disk are often subjected to complex loadings, including high rotational speeds and vibrations at high temperatures, and their failures are caused by a variety of mechanisms [5]. Therefore, it is worth studying efficient and reliable multiaxial fatigue life prediction methods. Considering the damage behavior of materials under multiaxial loading, many multiaxial fatigue models are proposed based on critical plane theory [6–8]. Currently, the application of neural networks has greatly promoted development in the field of fatigue life prediction [9–11].

Through decades of research, scholars have proposed many theoretical models for multiaxial fatigue life prediction. Several typical multiaxial fatigue models include the following: Smith et al. [12] proposed a model with the maximum normal strain plane as the critical plane, which takes the maximum normal strain range and the maximum normal stress on the critical plane as the fatigue damage parameters and has better prediction effects on the tensile materials. Kandil et al. [13] used the combination of shear strain and normal strain on the maximum shear strain plane to calculate the fatigue lives of materials. Taking the plane with the maximum shear strain amplitude as the critical plane, Fatemi et al. [14] proposed a critical plane model based on the shear strain and introduced the maximum normal stress on the critical plane to consider the influence of

normal stress. Shang et al. [15] took the maximum shear plane as the critical plane and proposed a critical plane model based on the equivalent strain. The above models were verified with experimental data and achieved better prediction effects. The experiment in Ref. [16] shows that the existence of non-zero mean stresses can reduce the life of a specimen under constant-amplitude loading. Although the above models have already realized the influences of the shear strain, normal strain, and normal stress on the critical plane for fatigue damage, they do not introduce shear stress. Thus, when predicting a specimen with mean shear stress using these models, their prediction results may be not accurate. Therefore, it is necessary to propose a new multiaxial fatigue theoretical model that comprehensively considers the influence of various variables on the critical plane, including the shear stress.

Since multiaxial fatigue theoretical models are developed based on the semi-empirical formula summarized from experimental data from some specific or limited materials, they may not generally reflect the mapping relationship between loading and fatigue life for other materials under different loadings and may lead to larger errors in the prediction of the specimen's life. Compared with multiaxial fatigue theoretical models, life prediction methods based on neural networks can effectively and autonomously learn the nonlinear mapping relationship between fatigue life and multiple variables from existing experimental data [17]. Yang et al. [11] proposed a prediction model based on deep learning. The principle is to take out a series of points on the loading path, use a long short-term memory neural network to establish an intermediate quantity closely related to the life from these points, and, finally, use a fully connected neural network to build a mapping relationship between the intermediate quantity and the fatigue life. Sun et al. [18] used a convolutional neural network to extract features from hysteresis images and capture information in the loading path for life prediction. In addition, Zhang et al. [19] developed a deep neural network model to predict life under creep-fatigue conditions. Feng et al. [20] established a convolutional neural network to predict the residual useful life of a structure. However, constructing a deep neural network is not easy for engineers and technicians who are not familiar with neural networks; it is valuable to establish a simple but effective network prediction model for engineering designers.

In practice, no matter what method is used to predict the life of a structure, both accuracy and convenience are important factors to be considered. A theoretical model has its specific theoretical formula, which facilitates the prediction of a structure's life. Usually, a neural network model that is trained enough could be more accurate for predicting a structure's life than a theoretical model. To provide engineers with more options, this study attempts to establish both a new theoretical model and a neural network model for fatigue prediction.

In order to comprehensively consider the influences of the critical plane variables on the fatigue damage and improve the prediction effect of the theoretical model, a new theoretical model (WYT) is proposed in this study, which takes the plane with the maximum shear strain amplitude as the critical plane and introduces the shear strain amplitude, normal strain range, maximum shear stress, and maximum normal stress as the main damage parameters simultaneously. To reduce the prediction error, a simple and convenient neural network framework is established. The shear strain amplitude, normal strain amplitude, mean shear stress, and mean normal stress on the critical plane are taken as the input parameters of the BPNN, and the fatigue life is taken as the output parameter. The fatigue lives of specimens under constant-amplitude and variable-amplitude loadings are predicted with the WYT model and the BPNN model, respectively. By comparing with the experimental results, it is proved that the WYT model is feasible, and the BPNN model is more accurate in predicting the fatigue lives of specimens. Finally, the influences of different variable groups as input parameters of the neural network on its prediction effect are discussed.

## 2. Stress–Strain Analysis under Multiaxial Loading

To describe the stress and strain states of a structure under multiaxial loading conditions, a smooth thin-walled tube and notched specimen are considered as the analysis objects.

### *2.1. Thin-Walled Tube under Multiaxial Loading*

The strain state of a point on a thin-walled tube under strain-controlled loading can be expressed as follows [21,22]:

$$\varepsilon = \begin{pmatrix} \varepsilon_x & \frac{\gamma_{xy}}{2} & 0 \\ \frac{\gamma_{yx}}{2} & -v_{eff}\varepsilon_x & 0 \\ 0 & 0 & -v_{eff}\varepsilon_x \end{pmatrix} \tag{1}$$

where $\varepsilon_x$ is the normal strain; $\gamma_{xy}$ is the shear strain, and $\gamma_{xy} = \gamma_{yx}$; $v_{eff}$ is the effective Poisson ratio, and $v_{eff} = 0.5 - \frac{(0.5-v_e)\Delta\sigma_{eq,a}}{E\Delta\varepsilon_{eq,a}}$ [21,22], where $v_e$ is the elastic Poisson ratio, $E$ is the elastic modulus, $\Delta\sigma_{eq,a}$ is the equivalent stress amplitude, and $\Delta\varepsilon_{eq,a}$ is the equivalent strain amplitude.

If the applied axial and shear strains are sinusoidal,

$$\varepsilon_x(t) = \varepsilon_{x,a}\sin\omega t + \varepsilon_{x,m} \tag{2}$$

$$\gamma_{xy}(t) = \gamma_{xy,a}\sin(\omega t - \varphi) + \gamma_{xy,m} \tag{3}$$

where $\varphi$ is the phase angle between the axial strain and shear strain. $\varepsilon_{x,a}$ and $\gamma_{xy,a}$ are the applied axial and shear strain amplitudes, respectively. $\varepsilon_{x,m}$ and $\gamma_{xy,m}$ are the applied mean axial and shear strains, respectively.

The shear strain and normal strain amplitudes on the maximum shear strain plane make an angle $\theta_c$ with the specimen axis, which can be expressed as [23]

$$\frac{\Delta\gamma_{\max}}{2} = \varepsilon_{x,a}\left\{\left[\lambda\cos(2\theta_c)\cos\varphi - (1+v_{eff})\sin(2\theta_c)\right]^2 + \left[\lambda\cos(2\theta_c)\sin\varphi\right]^2\right\}^{0.5} \tag{4}$$

$$\frac{\Delta\varepsilon_n}{2} = \frac{\varepsilon_{x,a}}{2}\left\{\left[2(1+v_{eff})\cos^2\theta_c + \lambda\sin(2\theta_c)\cos\varphi - 2v_{eff}\right]^2 + \left[\lambda\sin(2\theta_c)\sin\varphi\right]^2\right\}^{0.5} \tag{5}$$

where

$$\tan 4\theta_c = \frac{2\lambda(1+v_{eff})\cos\varphi}{(1+v_{eff})^2 - \lambda^2} \tag{6}$$

$$\lambda = \frac{\gamma_{xy,a}}{\varepsilon_{x,a}} \tag{7}$$

The critical plane is determined by taking the plane with the maximum shear strain amplitude as the critical plane. Supposing that two or more planes have the same maximum shear strain amplitude, the plane with the maximum normal strain range is considered as the critical plane. The calculation of various variables on the different planes can be found in Refs. [24–26].

### *2.2. Notched Specimen under Multiaxial Loading*

For a notched specimen under multiaxial loading, the stress and strain states at a point in the structure can be expressed as follows [27]:

$$\sigma = \begin{pmatrix} \sigma_x & \tau_{xy} & \tau_{xz} \\ \tau_{yx} & \sigma_y & \tau_{yz} \\ \tau_{zx} & \tau_{zy} & \sigma_z \end{pmatrix} \quad \varepsilon = \begin{pmatrix} \varepsilon_x & \varepsilon_{xy} & \varepsilon_{xz} \\ \varepsilon_{yx} & \varepsilon_y & \varepsilon_{yz} \\ \varepsilon_{zx} & \varepsilon_{zy} & \varepsilon_z \end{pmatrix} = \begin{pmatrix} \varepsilon_x & \frac{\gamma_{xy}}{2} & \frac{\gamma_{xz}}{2} \\ \frac{\gamma_{yx}}{2} & \varepsilon_y & \frac{\gamma_{yz}}{2} \\ \frac{\gamma_{zx}}{2} & \frac{\gamma_{zy}}{2} & \varepsilon_z \end{pmatrix} \tag{8}$$

where $\sigma_x$, $\sigma_y$, and $\sigma_z$ are normal stresses; $\tau_{xy}$, $\tau_{xz}$, $\tau_{yx}$, $\tau_{yz}$, $\tau_{zx}$, and $\tau_{zy}$ are shear stresses; $\varepsilon_x$, $\varepsilon_y$, and $\varepsilon_z$ are normal strains; $\gamma_{xy}$, $\gamma_{xz}$, $\gamma_{yx}$, $\gamma_{yz}$, $\gamma_{zx}$, and $\gamma_{zy}$ are shear strains; $\varepsilon_{xy}$, $\varepsilon_{xz}$, $\varepsilon_{yx}$, $\varepsilon_{yz}$, $\varepsilon_{yz}$, and $\varepsilon_{zy}$ are variable symbols related to $\gamma_{xy}$, $\gamma_{xz}$, $\gamma_{yx}$, $\gamma_{yz}$, $\gamma_{zx}$ and $\gamma_{zy}$, respectively, as follows: $\varepsilon_{xy} = \frac{\gamma_{xy}}{2}$, $\varepsilon_{xz} = \frac{\gamma_{xz}}{2}$, $\varepsilon_{yx} = \frac{\gamma_{yx}}{2}$, $\varepsilon_{yz} = \frac{\gamma_{yz}}{2}$, $\varepsilon_{zx} = \frac{\gamma_{zx}}{2}$, $\varepsilon_{zy} = \frac{\gamma_{zy}}{2}$.

The stress and strain components on any plane in a three-dimensional space can be obtained through a coordinate transformation as follows [7]:

$$\boldsymbol{\sigma}' = \boldsymbol{M}\boldsymbol{\sigma}\boldsymbol{M}^T \ \boldsymbol{\varepsilon}' = \boldsymbol{M}\boldsymbol{\varepsilon}\boldsymbol{M}^T \tag{9}$$

where $\boldsymbol{M}$ is the coordinate conversion matrix expressed as follows:

$$\boldsymbol{M} = \begin{pmatrix} \cos\theta\sin\phi & \sin\theta\sin\phi & \cos\phi \\ -\sin\theta & \cos\theta & 0 \\ -\cos\theta\cos\phi & -\sin\theta\cos\phi & \sin\phi \end{pmatrix} \tag{10}$$

As shown schematically in Figure 1, the angles $\theta$ and $\phi$ are the coordinate rotation angles. Any plane in a three-dimensional space can be obtained by changing angles $\theta$ and $\phi$, where $\theta$ increases from 0° to 360° by $\Delta\theta$ and $\phi$ increases from 0° to 180° by $\Delta\phi$.

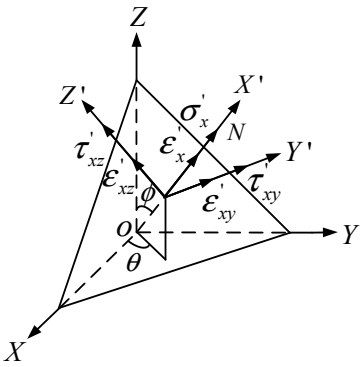


**Figure 1.** Stress and strain on any plane in three-dimensional coordinates adapted from Ref. [7].

For a notched specimen with stress concentration, the stress–strain response of the critical point should be obtained through finite element simulation, and then the stress–strain response on different planes is obtained through coordinate transformation. Finally, the plane with the maximum shear strain amplitude is taken as the critical plane.

## 3. Fatigue Life Prediction Model

### *3.1. A New Multiaxial Fatigue Model Based on the Critical Plane Theory*

The initiation of a fatigue crack is due to the local plastic deformation of a stable slip zone inside a material, and the direction of the stable slip zone is basically consistent with the direction of the maximum shear strain [28]. Therefore, it is reasonable to take the plane with the maximum shear strain amplitude as the critical plane.

Experiments show that cracks often initiate on the plane of maximum shear strain under different loadings [29,30]. Socie [31] proposed the use of the maximum shear strain amplitude $\frac{\Delta\gamma_{\max}}{2}$ as the main parameter affecting fatigue damage. Brown [29] believed that the normal strain $\varepsilon_n$ on the maximum shear strain plane also promotes crack propagation and used the maximum shear strain amplitude $\frac{\Delta\gamma_{\max}}{2}$ and maximum strain range $\Delta\varepsilon_n$ as the main parameters affecting multiaxial fatigue damage. Under non-proportional loading, the values and directions of principal stresses and principal strains change within a loading cycle, often causing additional cyclic hardening that reduces the life of the specimen [31]. However, models based entirely on strain cannot effectively describe the effect of additional cyclic hardening on multiaxial fatigue life under non-proportional loading. Fatemi [28] proposed that the maximum shear strain amplitude $\frac{\Delta\gamma_{\max}}{2}$ and the maximum normal stress $\sigma_{n,\max}$ on the maximum shear strain plane be used as the main

parameters affecting multiaxial fatigue damage, and the maximum normal stress could reflect the cyclic hardening caused by non-proportional loading. The experiments showed that the mean tensile stress perpendicular to the plane of maximum shear strain promoted crack growth, and the mean compressive stress delayed crack growth [32]. The existence of the mean shear stress reduces the life of a specimen under constant-amplitude loading [16]. Therefore, it is necessary to consider the influences of the normal stress and shear stress on fatigue damage simultaneously when establishing a multiaxial fatigue model. The stress–strain on a fatigue crack under tension–torsion loading is shown in Figure 2.

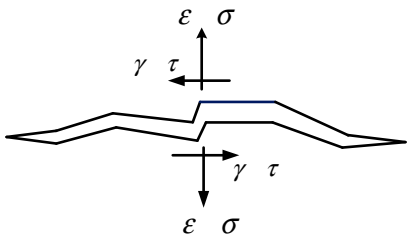


**Figure 2.** Schematic of stresses and strains on a fatigue crack adapted from Ref. [33].

To comprehensively consider the influences of stresses and strains on the critical plane on fatigue damage, this study takes the plane with the maximum shear strain amplitude as the critical plane and proposes a new multiaxial fatigue model based on the critical plane theory. The proposed new multiaxial fatigue model includes several parameters, including the maximum shear strain amplitude $\frac{\Delta\gamma_{\max}}{2}$ and the normal strain range $\Delta\varepsilon_n$ on the plane. Meanwhile, in order to consider the influences of stresses, normal stress and shear stress correction factors $\frac{\sigma_{n,\max}}{\sigma'_f}$ and $\frac{\tau_{\max}}{\tau'_f}$ [34] are also introduced. The newly proposed multiaxial fatigue model is expressed as follows:

$$\frac{\Delta\gamma_{\max}}{2}\left(1+\frac{\tau_{\max}}{\tau'_f}\right)+\Delta\varepsilon_n\left(1+\frac{\sigma_{n,\max}}{\sigma'_f}\right)=f\left(N_f\right) \tag{11}$$

where $\frac{\Delta\gamma_{\max}}{2}$ and $\Delta\varepsilon_n$ are introduced to take into account the influences of the shear strain and normal strain on crack propagation; $\frac{\tau_{\max}}{\tau'_f}$ is the normalization of the shear stress; the maximum shear stress $\tau_{\max}$ includes the mean shear stress, considering the influence of the mean shear stress on fatigue damage; $\frac{\sigma_{n,\max}}{\sigma'_f}$ is the normalization of the normal stress, considering the influence of additional cyclic hardening under non-proportional loading on fatigue damage, and the maximum normal stress $\sigma_{n,\max}$ includes the mean normal stress, considering the influence of the mean stress on crack propagation; $N_f$ is the fatigue life, i.e., the number of loading cycles when the specimen undergoes fatigue failure. $\tau'_f$ is the shear fatigue strength coefficient, and $\sigma'_f$ is the fatigue strength coefficient. The units of $\tau_{\max}$, $\tau'_f$, $\sigma_{n,\max}$, and $\sigma'_f$ are Pa.

In Ref. [35], $\frac{\Delta\gamma_{\max}}{2}$, $\Delta\varepsilon_n$, and $\sigma_{n,\max}$ are expressed as follows:

$$\begin{cases} \frac{\Delta\gamma_{\max}}{2}=(1+v_e)\frac{\sigma'_f}{E}\left(2N_f\right)^b+(1+v_p)\varepsilon'_f\left(2N_f\right)^c \\ \Delta\varepsilon_n=(1-v_e)\frac{\sigma'_f}{E}\left(2N_f\right)^b+(1-v_p)\varepsilon'_f\left(2N_f\right)^c \\ \sigma_{n,\max}=\frac{\sigma'_f}{2}\left(2N_f\right)^b \end{cases} \tag{12}$$

where $E$ is the elastic modulus of the material (unit: Pa); $\varepsilon'_f$ is the fatigue ductility coefficient; $b$ is the fatigue strength exponent; $c$ is the fatigue ductility exponent; $v_p$ is the plastic Poisson ratio of the material.

The maximum shear stress $\tau_{\max}$ on the critical plane can be expressed as follows [34]:

$$\tau_{\max} = \frac{\Delta\tau}{2} = \tau'_f \left(2N_f\right)^{b_0} \tag{13}$$

where $\frac{\Delta\tau}{2}$ is the shear stress amplitude; $b_0$ is the shear fatigue strength exponent.

For metallic materials, $v_e = 0.3$ and $v_p = 0.5$ [36]. Equations (12) and (13) are substituted into Equation (11) to obtain the following:

$$\begin{aligned} &\frac{\Delta\gamma_{\max}}{2}\left(1+\frac{\tau_{\max}}{\tau'_f}\right) + \Delta\varepsilon_n\left(1+\frac{\sigma_{n,\max}}{\sigma'_f}\right) = \left[1.3\frac{\sigma'_f}{E}\left(2N_f\right)^b + 1.5\varepsilon'_f\left(2N_f\right)^c\right] \\ &\times\left[1+\left(2N_f\right)^{b_0}\right] + \left[0.7\frac{\sigma'_f}{E}\left(2N_f\right)^b + 0.5\varepsilon'_f\left(2N_f\right)^c\right] \times \left[1+0.5\left(2N_f\right)^b\right] \end{aligned} \tag{14}$$

Based on the von Mises criterion [5], $b_0 = b$. Then, the right side of Equation (14) can be approximately expanded as follows:

$$\begin{aligned} \frac{\Delta\gamma_{\max}}{2}\left(1+\frac{\tau_{\max}}{\tau'_f}\right) + \Delta\varepsilon_n\left(1+\frac{\sigma_{n,\max}}{\sigma'_f}\right) = {} & 2\frac{\sigma'_f}{E}\left(2N_f\right)^b + 2\varepsilon'_f\left(2N_f\right)^c \\ & +1.65\frac{\sigma'_f}{E}\left(2N_f\right)^{2b} + 1.75\varepsilon'_f\left(2N_f\right)^{(b+c)} \end{aligned} \tag{15}$$

The mean value of the coefficients of $\frac{\sigma'_f}{E}\left(2N_f\right)^{2b}$ and $\varepsilon'_f\left(2N_f\right)^{(b+c)}$ in Equation (15) is considered, and Equation (14) can be approximately expressed as follows:

$$\begin{aligned} \frac{\Delta\gamma_{\max}}{2}\left(1+\frac{\tau_{\max}}{\tau'_f}\right) + \Delta\varepsilon_n\left(1+\frac{\sigma_{n,\max}}{\sigma'_f}\right) \approx {} & \left[\frac{\sigma'_f}{E}\left(2N_f\right)^b + \varepsilon'_f\left(2N_f\right)^c\right] \\ & \times\left[2+1.7\left(2N_f\right)^b\right] \end{aligned} \tag{16}$$

To distinguish it from other fatigue models, the multiaxial fatigue theoretical model proposed in this study is called the WYT model.

### *3.2. Establishment of a Neural Network Model*

Compared with the multiaxial fatigue theoretical model, a life prediction method based on neural networks can effectively and autonomously learn the nonlinear mapping relationships between fatigue life and multiple variables from existing experimental data, and it can better predict the fatigue life of a specimen under complex loading. With the advancement of data science, the application of deep neural networks has achieved better prediction effects on structural life prediction, but the construction of its complex network has brought great inconvenience, and it is rather difficult for engineers and technicians who are not familiar with neural networks. Therefore, the purpose of this section is to establish a simpler neural network method for predicting the lives of specimens under different types of loadings. BPNNs have a strong nonlinear adaptive ability, and they are widely used in life predictions for structures [37]. In this study, the variables of the critical plane are used as the input variables of the neural network so that the trained neural network can be used to predict the specimen lives under different types of loadings and can also predict the lives of some complex structures.

In this section, a BPNN model for predicting a specimen's life under multiaxial loading is established by combining the critical plane theory with a BPNN.

#### 3.2.1. Structure of a BPNN

A BPNN is a multilayer feedforward neural network; its main features are that the signal is the forward propagation, and the error is the backward propagation [38]. The training process of a BPNN is mainly divided into two stages. The first stage is the forward propagation of the signal, from the input layer to the hidden layer and, finally, to the output

layer; the second stage is the backpropagation of the error from the output layer to the hidden layer and, finally, to the input layer. If the output layer does not achieve the desired output, the error change value of the output layer is calculated, and then backpropagation is performed. The error signal is sent back through the network in reverse along the original connection path, and the weight of each layer of neurons is modified until the desired goal is achieved.

A BPNN usually has a three-layer structure as its typical form. These three-layer structures are usually the input layer, hidden layer, and output layer. Each layer may have multiple neurons; the neuron structures of each layer are basically the same, and the activation functions may be the same or different. The basic structure of a BPNN is shown in Figure 3.

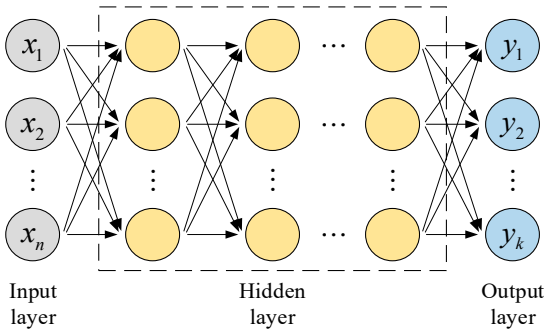


**Figure 3.** Structure of a BPNN adapted from Ref. [39].

The basic component unit of a neural network is a neuron, and the structure of a single neuron is shown in Figure 4. The output of a neuron is as follows [40]:

$$y = f\left(\sum_{i=1}^{n}(\omega_i x_i) + b\right) \tag{17}$$

where $f$ is the activation function; $\omega_i$ and $x_i$ are the weight and input value of the $i$-th input of the neuron, respectively; $b$ is the threshold of the neuron.

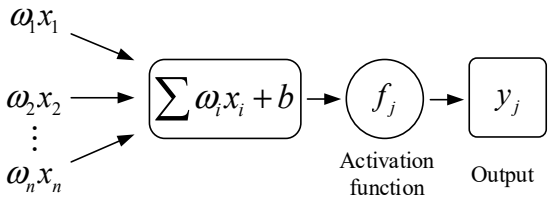


**Figure 4.** Structure of a single neuron reprinted from Ref. [40].

In theory, BPNN can approximate any nonlinear continuous function under the conditions of a reasonable structure and appropriate weight [41]. The flow of the BPNN algorithm is shown in Figure 5.

### 3.2.2. Establishment of a BPNN Model

The research in Refs. [36,42] shows that the shear strain and normal strain on the critical plane are important parameters affecting fatigue damage. Meanwhile, the experiment in Ref. [16] shows that the existence of non-zero mean stresses can also reduce the life of a specimen under constant-amplitude loading. The theoretical model proposed by Li et al. [25] directly introduced the mean shear stress and mean normal stress, and they verified their model by using the experimental data of some materials.

Inspired by the above research, when establishing a neural network, this study uses the shear strain amplitude $\frac{\Delta\gamma_{max}}{2}$, normal strain amplitude $\frac{\Delta\varepsilon_n}{2}$, mean shear stress $\tau_m$, and

mean normal stress $\sigma_m$ on the critical plane as the input parameters of the neural network and the life $N_f$ as the output parameter. The determination of the critical plane is detailed in Section 2. The BPNN model established in this study is shown in Figure 6, and its hyperparameter settings are shown in Table 1. The number of neurons in the hidden layer can be calculated by using the following formula [43]:

$$m = 2n + 1 \tag{18}$$

where $n$ is the number of neurons in the input layer.

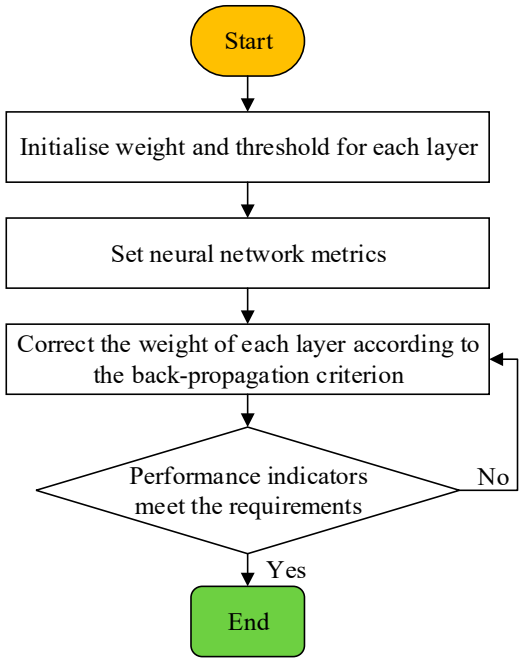


**Figure 5.** Flowchart of the BPNN algorithm.

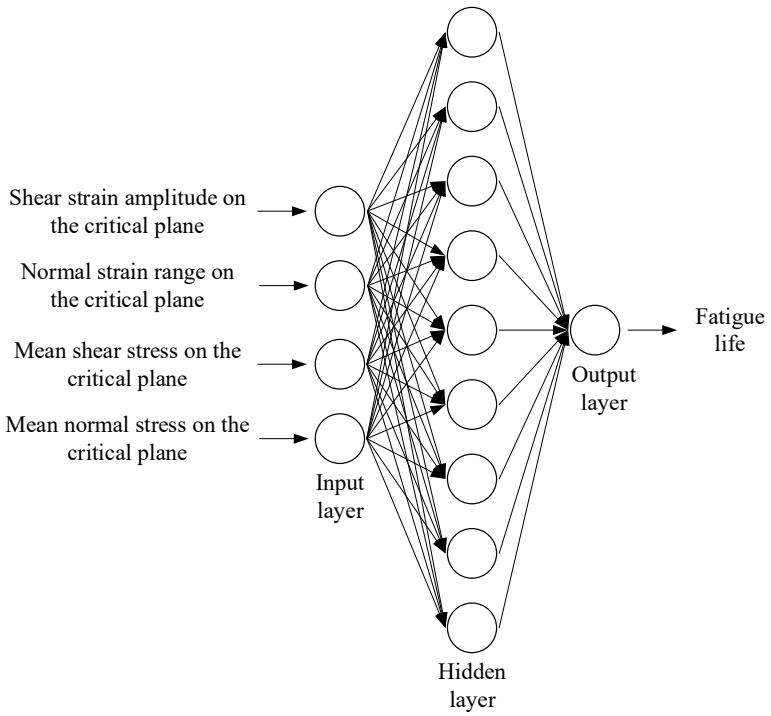


**Figure 6.** Structure of the BPNN model established in this study.

**Table 1.** Parameters of the BPNN model.

| Parameters | Settings |
|---|---|
| Neurons at the input layer | 4 |
| Neurons at the hidden layer | 9 |
| Neurons at the output layer | 1 |
| Activation function of the hidden layer | logsig |
| Activation function of the output layer | tansig |
| Training function | trainlm |
| Learning rate | 0.01 |

To facilitate the training of the BPNN model, the data need to be normalized. The formula is as follows [37]:

$$x = \frac{x_0 - x_{\min}}{x_{\max} - x_{\min}} \tag{19}$$

where $x_0$ is the original data, $x_{\min}$ is the minimum value of the original data, and $x_{\max}$ is the maximum value of the original data. When the final result is output, it should be de-normalized.

The BPNN model established in this study was realized using MATLAB R2019b Deep Learning Toolbox 13.0.

### *3.3. Existing Multiaxial Fatigue Theoretical Models*

In order to compare the prediction effects of the WYT model and the established BPNN model with other existing multiaxial fatigue models, this study sorts out two typical multiaxial fatigue theoretical models, as shown in Table 2. The model proposed by Smith [12] is called the SWT model, and the model proposed by Shang [15] is called the SHD model in this study. The SWT model takes the plane with the maximum normal strain amplitude as the critical plane and uses the product of the maximum normal strain amplitude and the normal stress on the plane as the damage parameter, without considering the influences of the shear stress and shear strain on the critical plane on fatigue damage. The SHD model takes the plane with the maximum shear strain amplitude as the critical plane and considers that the maximum shear strain amplitude and the normal strain range on the critical plane are the two main factors affecting the fatigue damage, without considering the effects of the shear stress and normal stress. Both the WYT model and the BPNN model proposed in this study consider the influences of stresses (shear stress and normal stress) and strains (shear strain and normal strain) on the critical plane for fatigue damage.

**Table 2.** Multiaxial fatigue models.

| | Models | Life Prediction Equations | References |
|---|---|---|---|
| 1 | SWT | $\sigma_{n,\max}\frac{\Delta\varepsilon_n}{2} = f(N_f)$ | [12] |
| 2 | SHD | $\left[\Delta\varepsilon_n^{*2} + \frac{1}{3}(\Delta\gamma_{\max}/2)^2\right]^{1/2} = f(N_f)$ | [15] |

## 4. Experimental Data Verification

In order to compare the prediction effects of the four models (the WYT model, BPNN model, SWT model, and SHD model) for different material specimens under constant-amplitude loading and variable-amplitude loading, the experimental data of S45C steel [44] and 7075-T651 aluminum alloy [45,46] are selected for life predictions in this study.

### *4.1. Life Prediction of the Two Material Specimens under Constant-Amplitude Loading*

The two material specimens are both smooth thin-walled tubes, as shown in Figure 7. The fatigue properties of each material are shown in Table 3. The loading mode of each material specimen is sine-wave loading; the loading paths are shown in Figure 8, and

the detailed experimental data are shown in Appendix A and Appendix B. The detailed experimental processes of the two material specimens can be found in Refs. [44,45].

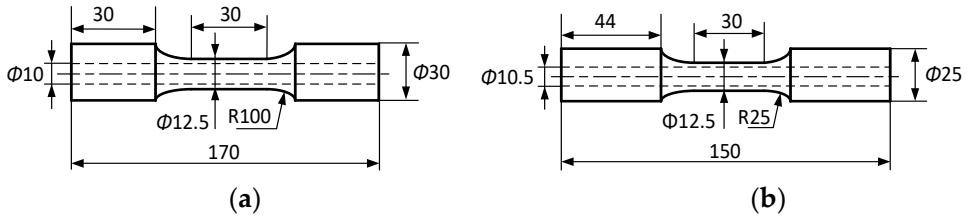


**Figure 7.** Specimen dimensions (unit: mm). (**a**) S45C reprinted from Ref. [47]; (**b**) 7075-T651 reprinted from Ref. [45].

**Table 3.** Material fatigue properties.

| Properties | Symbols | S45C [44] | 7075-T651 [45,48] |
|---|---|---|---|
| Modulus of elasticity | $E$ (GPa) | 186 | 71.7 |
| Shear modulus | $G$ (GPa) | 73 | 27.5 |
| Yield strength | $\sigma_y$ (MPa) | 496 | 501 |
| Ultimate tensile strength | $\sigma_u$ (MPa) | 770 | 561 |
| Fatigue strength coefficient | $\sigma_f'$ (MPa) | 1206 * | 1235 |
| Fatigue ductility coefficient | $\varepsilon_f'$ | 0.29 * | 0.243 |
| Fatigue strength exponent | $b$ | −0.09 * | −0.138 |
| Fatigue ductility exponent | $c$ | −0.56 * | −0.71 |
| Shear fatigue strength coefficient | $\tau_f'$ (MPa) | 696 * | 797 |
| Shear fatigue ductility coefficient | $\gamma_f'$ | 0.5 * | 5.42 |
| Shear fatigue strength exponent | $b_0$ | −0.09 * | −0.126 |
| Shear fatigue ductility exponent | $c_0$ | −0.56 * | −1.173 |

* The uniaxial fatigue parameters of S45C are estimated based on the Muralidharan–Manson method in Ref. [49], and the torsional fatigue parameters can be estimated from the corresponding uniaxial fatigue parameters by using the von Mises criterion [5].

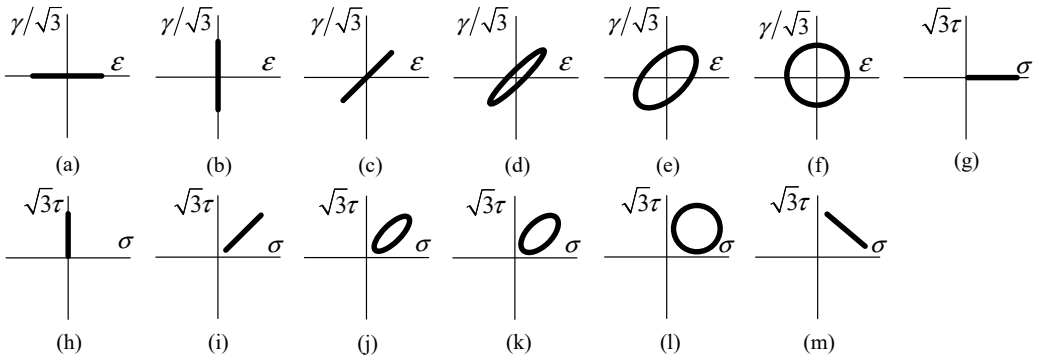


**Figure 8.** Loading paths considered in this study adapted from Refs. [21,45]. (**a**) is axial loading; (**b**) is torsional loading; (**c**) is proportional loading; (**d**–**f**) are non-proportional loading; (**g**) is axial loading, the mean normal stress is not zero; (**h**) is torsional loading, the mean shear stress is not zero; (**i**) is proportional loading, the mean normal stress and mean shear stress are not zero; (**j**–**m**) are non-proportional loading, the mean normal stress and mean shear stress are not zero.

To verify the generalization ability of the BPNN model's prediction (prediction ability on unknown data), eighty percent of the data in each material are used as the training set, twenty percent of the data are used as the test set, i.e., nineteen groups of experimental data for S45C are used as the training set, and five groups of experimental data are used as the test set (the bolded experimental data in Appendix A); forty-two groups of experimental data for 7075-T651 are used as the training set, and ten groups of experimental data are used

as the test set (the bolded experimental data in Appendix B). In this section, the trained BPNN with the four input parameters ($\frac{\Delta\gamma_{\max}}{2}$, $\frac{\Delta\varepsilon_n}{2}$, $\tau_{\mathrm{m}}$, $\sigma_m$) is called the BPNN model.

#### 4.1.1. Life Prediction

The mechanical properties and fatigue parameters of the two materials are given in Table 3. According to the experimental data in Sections A and B, the SWT model, SHD model, WYT model, and BPNN model are used to predict the fatigue lives of the two material specimens under constant-amplitude loading, and the prediction results are shown in Figures 9 and 10. To visually see the distribution of the prediction results of each model, their distributions in the error band are counted, as shown in Tables 4 and 5.

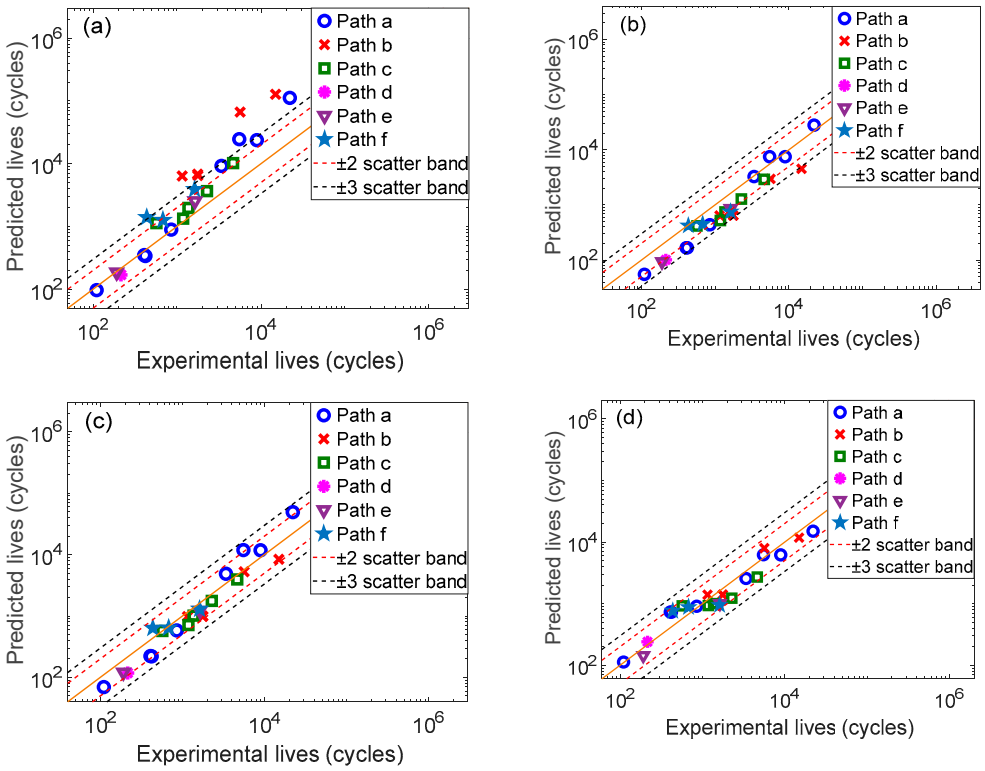


**Figure 9.** Predicted lives of each model for S45C: (**a**) SWT, (**b**) SHD, (**c**) WYT, and (**d**) BPNN.

**Table 4.** Distributions of the prediction results for S45C using different models within the error band.

| Scatter Band | SWT | SHD | WYT | BPNN |
|---|---|---|---|---|
| ±3 | 66.67% | 95.83% | 100% | 100% |
| ±2 | 50% | 62.5% | 91.67% | 100% |

**Table 5.** Distribution of the prediction results for 7076-T651 using different models within the error band.

| Scatter Band | SWT | SHD | WYT | BPNN |
|---|---|---|---|---|
| ±3 | 53.85% | 57.69% | 75% | 100% |
| ±2 | 32.69% | 36.54% | 48.08% | 86.54% |

It can be seen from Figure 9 and Table 4 that the best prediction effect for S45C is that of the BPNN model, and the prediction results are all within the two-time error band in Figure 9d. The second is that of the WYT mode, and most of the results are within the two-time error band in Figure 9c. The prediction effect of the SHD model for S45C is also better, with only one data point outside the three-time error band in Figure 9b. However,

the SWT model has a poorer prediction effect on S45C, and some data points are outside the three-time error band in Figure 9a.

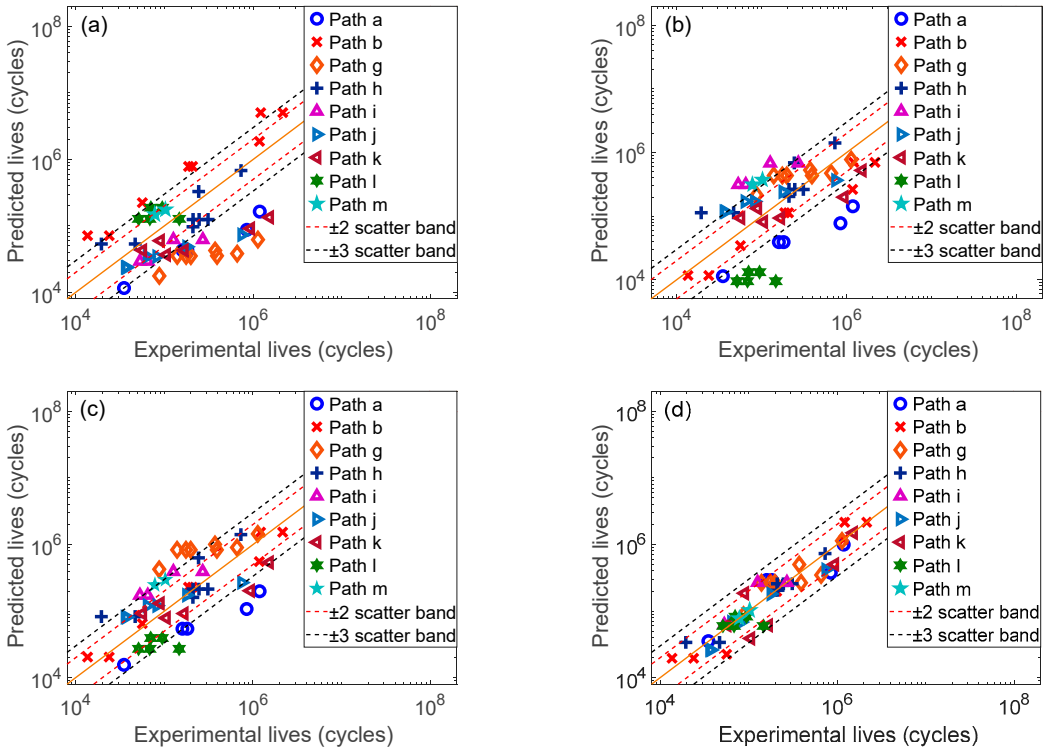


**Figure 10.** Predicted lives of each model for 7075-T651: (**a**) SWT, (**b**) SHD, (**c**) WYT, and (**d**) BPNN.

Based on Figure 10 and Table 5, it can be seen that the best prediction effect for 7075-T651 is that of the BPNN model, and all of the prediction results are within the three-time error band in Figure 10d. The second is that of the WYT model, for which most of the data points are within the three-time error band in Figure 10c. However, almost half of the data points of the SWT model and the SHD model are outside the three-time error band in Figure 10a,b.

#### 4.1.2. Prediction Result Analysis

The experimental data of the two material specimens are used to evaluate the prediction effects of the four models, and it can be found that the prediction results of different models for the same material specimens are different.

The SWT model considers the normal strain and maximum normal stress on the critical plane, which can reflect the effect of the non-proportional additional strengthening phenomenon on fatigue life [50]. However, the SWT model does not consider the effect of shear stress, so it has a poor prediction effect for 7075-T651 and has a poor prediction effect for S45C under loading paths a, b, and f. The SHD model uses the von Mises criterion to synthesize an equivalent damage parameter from the shear strain amplitude and normal strain range on the critical plane, and it has a better prediction effect for S45C. Since the fatigue damage parameter of the SHD model is just based on strains and does not consider the effects of stresses on fatigue damage, its prediction results for S45C are conservative, and for the same reason, it has poorer prediction effects for 7075-T651. Since the WYT model considers the influences of both the strains and the stresses on the critical plane simultaneously, it has better prediction effects for S45C and 7075-T651.

Compared with the three theoretical models (the SWT model, the SHD model, and the WYT model), the BPNN model in this study does not need a detailed derivation process and has a simple structure, and the results of the training set and the test set for each material are within the three-time error band.

### *4.2. Life Prediction of the Two Material Specimens under Variable-Amplitude Loading*

To evaluate the prediction effects of the above four models on specimens of different materials under variable-amplitude loading, the fatigue lives of S45C and 7075-T651 specimens under variable-amplitude loading are predicted. When predicting the specimen life under variable-amplitude loading, it is necessary to count the variables in the time domain on the critical plane using the multiaxial rainflow counting method [51,52] and to record the strain and stress results of each cycle by using a model to predict the fatigue damage under each cycle's loading. Based on the linear Palmgren–Miner damage accumulation rule, the total fatigue damage of the specimen under variable-amplitude loading is

$$D = \sum_{i=1}^{n} \frac{1}{N_{fi}} \tag{20}$$

where $n$ is the number of cycles, and $N_{fi}$ is the fatigue life corresponding to the i-th cycle. Fatigue failure occurs when $D = 1$.

#### 4.2.1. Life Prediction of the S45C Steel Specimen under Variable-Amplitude Loading in the Time Domain

The S45C steel specimen is a thin-walled tube, as shown in Figure 7, and the time histories of strains are given in Ref. [44]. Based on the experimental data of S45C under variable-amplitude loading in Ref. [44], the four models are used to predict the life of the S45C specimen, and the prediction results are shown in Figure 11. To visually see the distribution of the prediction results of each model, their distributions in the error band are counted, as shown in Table 6.

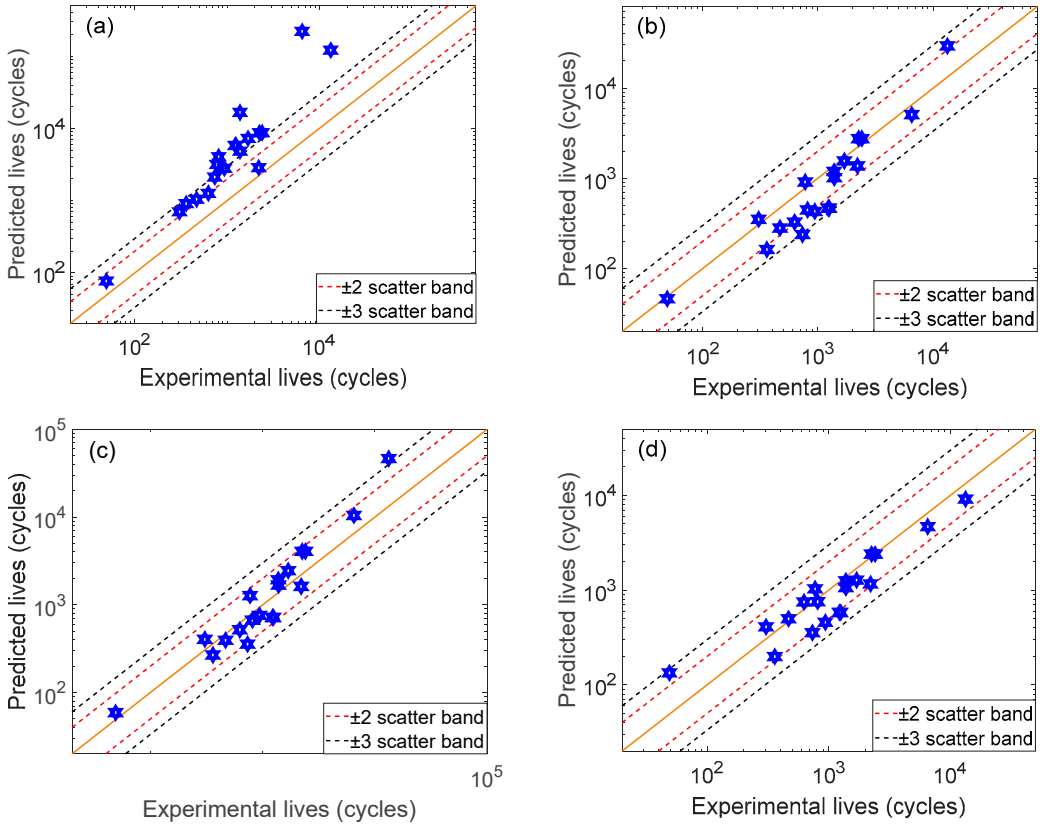


**Figure 11.** Predicted lives of each model for S45C under variable-amplitude loading: (**a**) SWT, (**b**) SHD, (**c**) WYT, and (**d**) BPNN.

**Table 6.** Distribution of the prediction results for S45C under variable-amplitude loading using different models within the error band.

| Scatter Band | SWT | SHD | WYT | BPNN |
|---|---|---|---|---|
| ±3 | 42% | 94.74% | 94.74% | 100% |
| ±2 | 10.53% | 68.42% | 89.47% | 73.68 |

According to Figure 11 and Table 6, it can be seen that the BPNN model has the best prediction effect for S45C, and the prediction results are all within the three-time error band in Figure 11d. It is followed by the SHD model and WYT model, each of them has only one data point outside the three-time error band in Figure 11b,c. However, the SWT model has a poor prediction effect for S45C, with almost half of the data points being outside the three-time error band in Figure 11a.

The calculation results show that the WYT model is feasible. By combining the critical plane method with the neural network, the BPNN model takes the variables on the critical plane as its input parameters, and its prediction effect is the best.

#### 4.2.2. Life Prediction of the 7075-T651 Aluminum Alloy Specimen under Random-Vibration Loading in the Frequency Domain

The 7075-T651 aluminum alloy notched specimen [46] is shown in Figure 12, and the material properties are shown in Table 3. The loading acceleration power spectral densities and experimental life results are shown in Table 7. The acceleration power spectral density (PSD) diagram is shown in Figure 13. During the experiment, one end of the specimen is fixed on a vibration table horizontally with a clamp and is subjected to vertical random vibration acceleration excitation. The detailed experimental process can be found in Ref. [46].

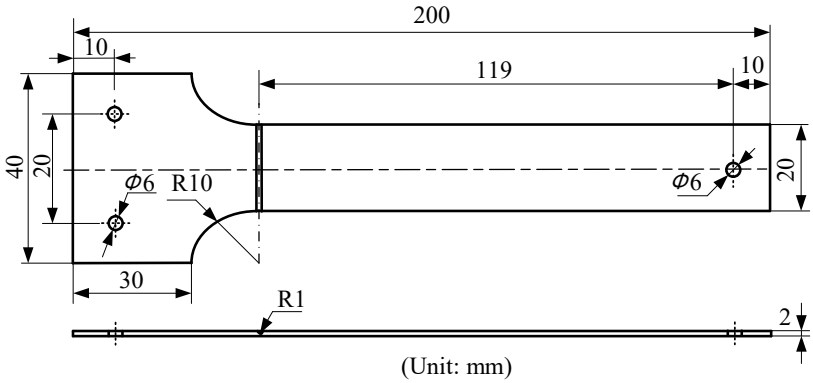


**Figure 12.** Schematic diagram of the specimen's dimensions adapted from Ref. [46].

**Table 7.** Acceleration power spectral densities and experimental life results of the 7075-T651 specimens under random-vibration loading adapted from Ref. [46].

| Specimen No. | $\xi_1$ ($g^2$/Hz) | $\xi_2$ ($g^2$/Hz) | $f_{min}$ (Hz) | $f_{mid}$ (Hz) | $f_{max}$ (Hz) | Excitation Direction | Experimental Lives (s) |
|---|---|---|---|---|---|---|---|
| 1 | 0.025 | 0.025 | 10 | - | 400 | Z | 13,032 |
| 2 | 0.05 | 0.05 | 10 | - | 400 | Z | 2196 |
| 3 | 0.075 | 0.075 | 10 | - | 400 | Z | 1326 |
| 4 | 0.02 | 0.15 | 10 | 150 | 350 | Z | 15,210 |
| 5 | 0.05 | 0.15 | 10 | 150 | 350 | Z | 1380 |
| 6 | 0.075 | 0.15 | 10 | 150 | 350 | Z | 1032 |
| 7 | 0.03 | 0.025 | 10 | 150 | 350 | Z | 7974 |
| 8 | 0.06 | 0.025 | 10 | 150 | 350 | Z | 1710 |
| 9 | 0.08 | 0.025 | 10 | 150 | 350 | Z | 534 |

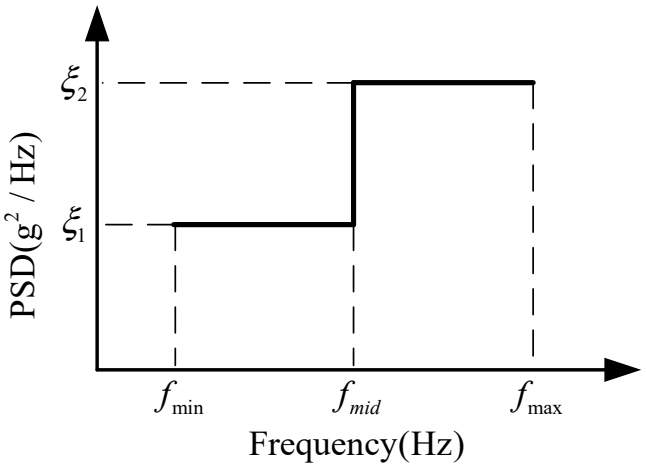


**Figure 13.** Acceleration excitation PSD.

(1) Finite Element Simulation

The dimensions of the 7075-T651 specimen are known, and finite element modeling is performed, as shown in Figure 14. The first-order and second-order structural natural frequencies of the specimen are shown in Table 8, and the relative errors between the frequencies in the simulation and the experiment are less than 5%. The stress contour diagram, PSD responses, and time histories are presented for the 7075-T651 specimen shown in Figures 15–17, respectively. It can be seen from Figure 16 that the peak frequencies of the response PSD functions of the specimen almost coincide with the first-order and second-order natural frequencies in Table 8. However, due to the limited length of this paper, the PSD responses under all conditions are not shown one by one, and only the stress time responses in the X and Y directions under the PSD amplitude of 0.025 $g^2$/Hz loading are drawn in Figure 17. In this study, the sampling frequency is set to 20 times the highest frequency of excitation (400 Hz) for the specimen, and the response time histories of 10 *s* are obtained by using the inverse fast Fourier transform (IFFT), and the number of sampling points for the 7075-T651 aluminum alloy specimen is 80,000 in Figure 17.

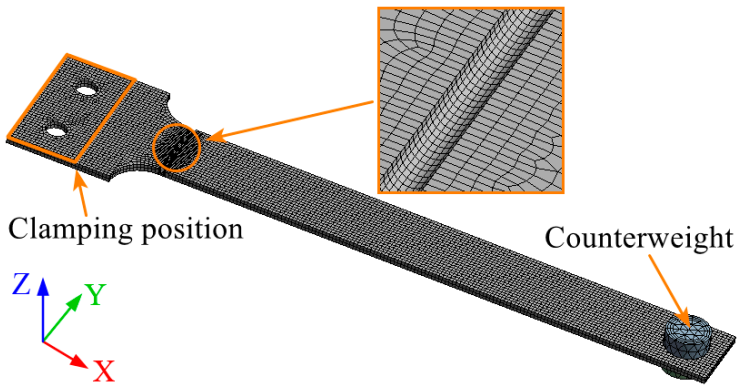


**Figure 14.** Finite element model of the specimen.

**Table 8.** Frequency comparisons.

| First-Order Natural Frequency | | Second-Order Natural Frequency | |
|---|---|---|---|
| **Experiment Frequency** | **Simulation Frequency** | **Experiment Frequency** | **Simulation Frequency** |
| 30.7 Hz | 30.4 Hz | 262.2 Hz | 269.2 Hz |

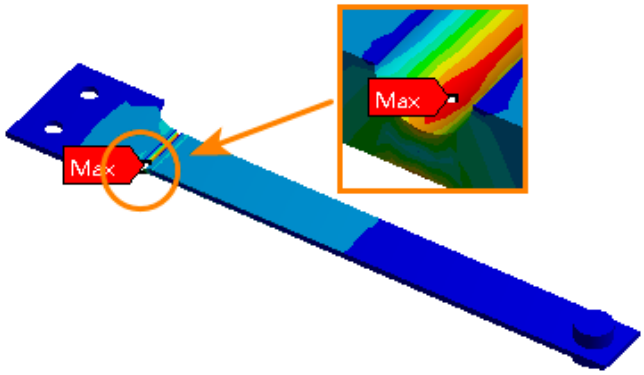


**Figure 15.** Stress contour diagram of the 7075-T651 aluminum alloy specimen.

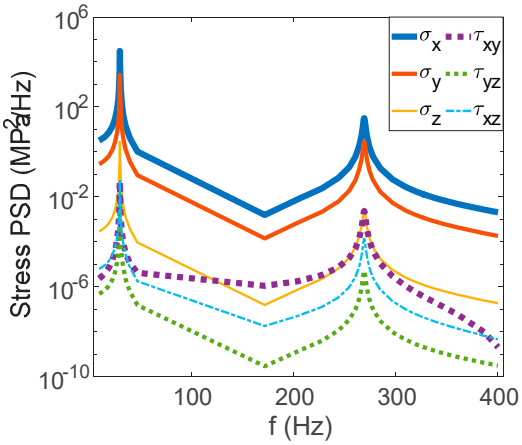


**Figure 16.** Stress PSD responses of the specimen at the maximum von Mises stress point under the PSD amplitude of 0.025 $g^2$/Hz loading.

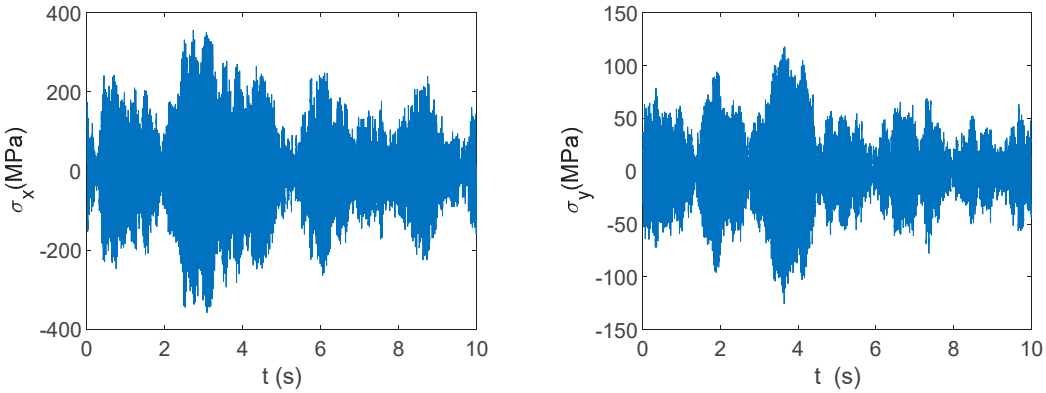


**Figure 17.** Stress time histories of the specimen at the maximum von Mises stress point under the PSD amplitude of 0.025 $g^2$/Hz loading.

(2) Life Prediction

Based on the simulation results under PSD loadings with different amplitudes, all four models are used to predict the life of the notched 7075-T651 specimen. The lives are calculated repeatedly for each loading spectrum ten times to take the mean value, and the prediction results are shown in Figure 18. To visually see the distribution of the prediction results of each model, their distributions in the error band are counted, as shown in Table 9.

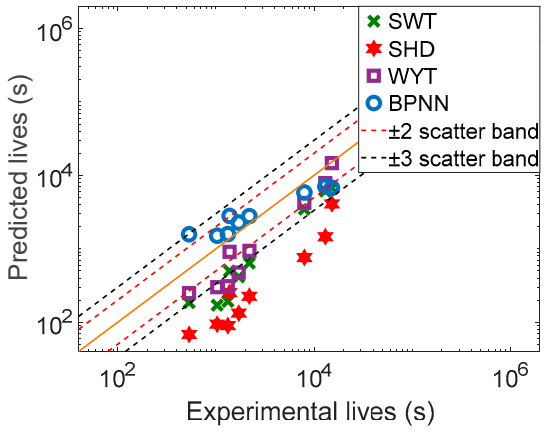


**Figure 18.** Life prediction results of the four models for the notched 7075-T651 specimen under random-vibration loading.

**Table 9.** Distribution of the prediction results for 7075-T651 under random-vibration loading using different models within the error band.

| Scatter Band | SWT | SHD | WYT | BPNN |
|---|---|---|---|---|
| ±3 | 55.56% | 0% | 66.67% | 100% |
| ±2 | 0% | 0% | 44.44% | 66.67% |

According to Figure 18 and Table 9, it can be seen that the BPNN model has the best prediction effect on the 7075-T651 specimen, and the predicted results are all within the three-time error band. The second is the WYT model, but some of its points are outside the three-time error band. The prediction points of the SWT model and the SHD model are almost outside the three-time error band. The prediction effects of the four models in predicting the life of the notched 7075-T651 specimen are ranked as follows: BPNN model, WYT model, SWT model, and SHD model.

The calculation results in Sections 4.1 and 4.2 show that the WYT model and established BPNN model are feasible, and they can predict not only the life of a specimen under constant-amplitude loading but also the fatigue life of a specimen under variable-amplitude loading.

## 5. Discussion

In order to study the influences of different forms of input parameters on the prediction effect of the BPNN model, this section selects three different variable groups as the input parameters of the BPNN model, namely, ($\frac{\Delta\gamma_{max}}{2}$, $\sigma_{n,max}$), ($\frac{\Delta\gamma_{max}}{2}$, $\frac{\Delta\varepsilon_n}{2}$, $\sigma_{n,max}$), and ($\frac{\Delta\gamma_{max}}{2}$, $\frac{\Delta\varepsilon_n}{2}$, $\tau_{max}$, $\sigma_{n,max}$). The BPNN model with three different variable groups is trained by using the experimental data of S45C and 7075-T651 under constant-amplitude loading. The dataset division is detailed in Section 4.1. The calculation results of the BPNN model with three different variable groups for the two materials under constant-amplitude loading are shown in Figure 19. To visually see the distribution of the prediction results of the BPNN model with three different variable groups, the distributions in the error band are counted, as shown in Tables 10 and 11.

**Table 10.** Distribution of the prediction results for S45C using the BPNN model with different input parameters within the error band.

| Scatter Band | BPNN Model with Two Input Parameters ($\frac{\Delta\gamma_{max}}{2}$, $\sigma_{n,max}$) | BPNN Model with Three Input Parameters ($\frac{\Delta\gamma_{max}}{2}$, $\frac{\Delta\varepsilon_n}{2}$, $\sigma_{n,max}$) | BPNN Model with Four Input Parameters ($\frac{\Delta\gamma_{max}}{2}$, $\frac{\Delta\varepsilon_n}{2}$, $\tau_{max}$, $\sigma_{n,max}$) |
|---|---|---|---|
| ±3 | 100% | 100% | 100% |
| ±2 | 100% | 100% | 100% |

**Table 11.** Distribution of the prediction results for 7075-T651 using the BPNN model with different input parameters within the error band.

| Scatter band | BPNN Model with Two Input Parameters ($\frac{\Delta\gamma_{max}}{2}$, $\sigma_{n,max}$) | BPNN Model with Three Input Parameters ($\frac{\Delta\gamma_{max}}{2}$, $\frac{\Delta\varepsilon_n}{2}$, $\sigma_{n,max}$) | BPNN Model with Four Input Parameters ($\frac{\Delta\gamma_{max}}{2}$, $\frac{\Delta\varepsilon_n}{2}$, $\tau_{max}$, $\sigma_{n,max}$) |
|---|---|---|---|
| ±3 | 94.23% | 88.46% | 100% |
| ±2 | 69.23% | 75% | 82.69 |

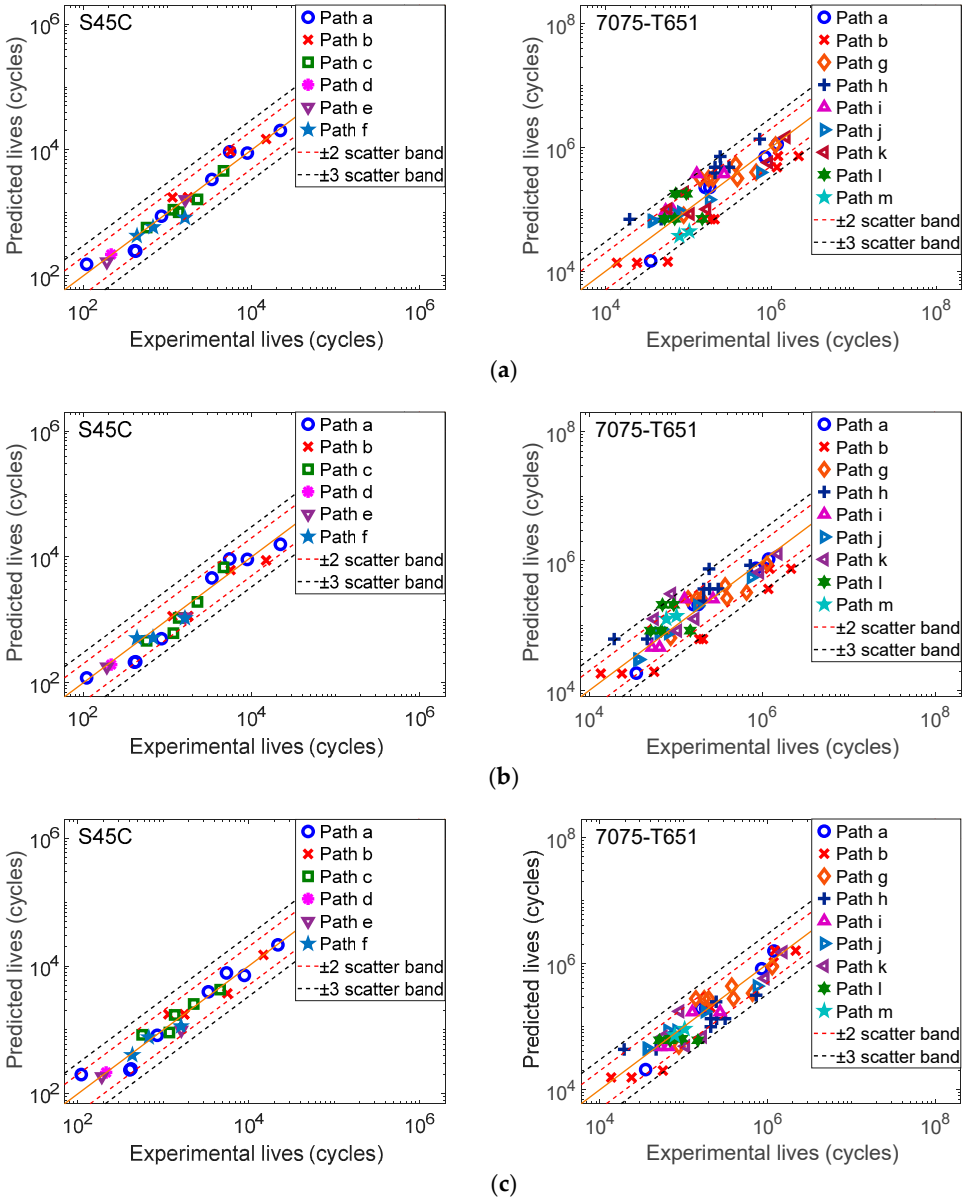


**Figure 19.** Predicted lives of the BPNN model with different variable groups for two material specimens. (**a**) Predicted lives of the BPNN model with two input parameters ($\frac{\Delta\gamma_{max}}{2}$, $\sigma_{n,max}$) for S45C and 7075-T651. (**b**) Predicted lives of the BPNN model with three input parameters ($\frac{\Delta\gamma_{max}}{2}$, $\frac{\Delta\varepsilon_n}{2}$, $\sigma_{n,max}$) for S45C and 7075-T651. (**c**) Predicted lives of the BPNN model with four input parameters ($\frac{\Delta\gamma_{max}}{2}$, $\frac{\Delta\varepsilon_n}{2}$, $\tau_{max}$, $\sigma_{n,max}$) for S45C and 7075-T651.

For S45C, based on Figure 19 and Table 10, when the three variable groups ($\frac{\Delta\gamma_{max}}{2}$, $\sigma_{n,max}$), ($\frac{\Delta\gamma_{max}}{2}$, $\frac{\Delta\varepsilon_n}{2}$, $\sigma_{n,max}$), and ($\frac{\Delta\gamma_{max}}{2}$, $\frac{\Delta\varepsilon_n}{2}$, $\tau_{max}$, $\sigma_{n,max}$) are taken as input parameters of the BPNN model, the BPNN model has a better prediction effect, and the prediction results are all within the two-time error band. Its prediction effect is similar to that of the BPNN

model with four input parameters ($\frac{\Delta\gamma_{max}}{2}$, $\frac{\Delta\varepsilon_n}{2}$, $\tau_m$, $\sigma_m$) and better than that of the three theoretical models in Section 4.1.1.

For 7075-T651, based on Figure 19 and Table 11, the BPNN model with two input parameters ($\frac{\Delta\gamma_{max}}{2}$, $\sigma_{n,max}$) or three input parameters ($\frac{\Delta\gamma_{max}}{2}$, $\frac{\Delta\varepsilon_n}{2}$, $\sigma_{n,max}$) has a better prediction effect, and the prediction results are almost within the three-time error band, making them better than those of the three theoretical models in Section 4.1.1, but the prediction effects are not better than that of the BPNN model with four input parameters ($\frac{\Delta\gamma_{max}}{2}$, $\frac{\Delta\varepsilon_n}{2}$, $\tau_m$, $\sigma_m$). The prediction effect of the BPNN model with four input parameters ($\frac{\Delta\gamma_{max}}{2}$, $\frac{\Delta\varepsilon_n}{2}$, $\tau_{max}$, $\sigma_{n,max}$) for 7075-T651 is similar to that of the BPNN model with four input parameters ($\frac{\Delta\gamma_{max}}{2}$, $\frac{\Delta\varepsilon_n}{2}$, $\tau_m$, $\sigma_m$), and the prediction results are all within the three-time error band.

Ref. [28] points out that it is reasonable to take the plane with the maximum shear strain amplitude as the critical plane. The variables on the maximum shear strain plane are taken as the input parameters of the BPNN in this study. Meanwhile, the BPNN can effectively and autonomously learn the nonlinear mapping relationships between fatigue life and multiple variables from existing experimental data, so the trained BPNN model can better predict the specimen's life.

For S45C, the mean shear stress and mean normal stress of all loading paths are zero, and the life of the specimen is not affected by mean stresses. Therefore, when ($\frac{\Delta\gamma_{max}}{2}$, $\sigma_{n,max}$), ($\frac{\Delta\gamma_{max}}{2}$, $\frac{\Delta\varepsilon_n}{2}$, $\sigma_{n,max}$), ($\frac{\Delta\gamma_{max}}{2}$, $\frac{\Delta\varepsilon_n}{2}$, $\tau_{max}$, $\sigma_{n,max}$), and ($\frac{\Delta\gamma_{max}}{2}$, $\frac{\Delta\varepsilon_n}{2}$, $\tau_m$, $\sigma_m$) are used as input parameters of the BPNN, their prediction effects on S45C are similar, and the prediction results are all within the two-time error band.

For 7075-T651, there are situations in the loading paths where the mean shear stress and mean normal stress are not zero. At this time, the life of the specimen is affected by mean stresses. However, the BPNN model with two input parameters ($\frac{\Delta\gamma_{max}}{2}$, $\sigma_{n,max}$) or three input parameters ($\frac{\Delta\gamma_{max}}{2}$, $\frac{\Delta\varepsilon_n}{2}$, $\sigma_{n,max}$) does not consider the influences of mean stresses simultaneously, and the prediction results for 7075-T651 are not all within the three-time error band. The BPNN model with four input parameters ($\frac{\Delta\gamma_{max}}{2}$, $\frac{\Delta\varepsilon_n}{2}$, $\tau_{max}$, $\sigma_{n,max}$) or four input parameters ($\frac{\Delta\gamma_{max}}{2}$, $\frac{\Delta\varepsilon_n}{2}$, $\tau_m$, $\sigma_m$) considers the influences of mean stresses simultaneously, and the prediction results of 7075-T651 are all within the three-time error band.

The calculation results in Section 5 show that taking different variable groups as input parameters of the BPNN model makes its prediction effects different. Therefore, we should pay attention to the selection of input parameters when training the BPNN model.

## 6. Conclusions

(1) In Section 3.1, the WYT model not only considers the influences of shear strain and normal strain on the critical plane but also those of normal stress and shear stress. By predicting the lives of two material specimens under constant-amplitude and variable-amplitude loading, respectively, in Section 4, the WYT model has better prediction effects for the two material specimens than the SWT model and SHD model based on Tables 4–6 and 9.

(2) In Section 3.2, a BPNN model with four input parameters ($\frac{\Delta\gamma_{max}}{2}$, $\frac{\Delta\varepsilon_n}{2}$, $\tau_m$, $\sigma_m$) for multiaxial fatigue life prediction is established by using the shear strain amplitude, normal strain amplitude, mean shear stress, and mean normal stress on the critical plane as input variables of the BPNN. In Section 4, the prediction effect of the trained BPNN model with four input parameters ($\frac{\Delta\gamma_{max}}{2}$, $\frac{\Delta\varepsilon_n}{2}$, $\tau_m$, $\sigma_m$) is better than that of the WYT model for the same material specimen based on Tables 4–6 and Table 9. This is because the BPNN model can effectively and autonomously learn the nonlinear mapping relationships between fatigue life and multiple variables from existing experimental data, which is its advantage.

(3) In Section 5, the influences of different variable groups as input parameters of the neural network on the prediction effect are discussed. Two variables ($\frac{\Delta\gamma_{max}}{2}$, $\sigma_{n,max}$), three variables ($\frac{\Delta\gamma_{max}}{2}$, $\frac{\Delta\varepsilon_n}{2}$, $\sigma_{n,max}$), and four variables ($\frac{\Delta\gamma_{max}}{2}$, $\frac{\Delta\varepsilon_n}{2}$, $\tau_{max}$, $\sigma_{n,max}$) are

used as the input parameters of the BPNN model. Their effects for the two material specimens are better than those of the three theoretical models (SWT, SHD, and WYT) based on Tables 4, 5, 10 and 11; the prediction results of the BPNN model with four input parameters ($\frac{\Delta\gamma_{max}}{2}$, $\frac{\Delta\varepsilon_n}{2}$, $\tau_{max}$, $\sigma_{n,max}$) and the BPNN model with four input parameters ($\frac{\Delta\gamma_{max}}{2}$, $\frac{\Delta\varepsilon_n}{2}$, $\tau_m$, $\sigma_m$) for S45C are both within the two-time error band based on Tables 4 and 10; the prediction results of the BPNN model with four input parameters ($\frac{\Delta\gamma_{max}}{2}$, $\frac{\Delta\varepsilon_n}{2}$, $\tau_{max}$, $\sigma_{n,max}$) and the BPNN model with four input parameters ($\frac{\Delta\gamma_{max}}{2}$, $\frac{\Delta\varepsilon_n}{2}$, $\tau_m$, $\sigma_m$) for 7075-T651 are both within the three-time error band based on Tables 5 and 11.

(4) Although the prediction effect of the WYT model is not better than that of the BPNN model for the same material specimen, it is better than those reported earlier. On the contrary, the construction of neural network models is not easy for engineers and technicians who are not familiar with neural networks. The purpose of this study is to provide more options for engineers when predicting a structural life under different loadings.

(5) This study uses small-sample data to train the proposed BPNN model. If more test data are used to train the BPNN model, it is believed that its prediction accuracy may be further improved. If the WYT model is to be used to simulate and calculate life data under different loading conditions, and these are used to train the BPNN model, the effect of the trained BPNN model on the prediction of the life of a specimen needs further study.

**Author Contributions:** Conceptualization, Y.W. and Y.Q.; methodology, Y.W. and J.L.; software, Y.W. and J.B.; validation, Y.W. and Y.Q.; formal analysis, Y.Q.; investigation, J.B.; resources, J.L.; data curation, Y.W. and Y.Q.; writing—original draft preparation, Y.W.; writing—review and editing, Y.Q. and J.L.; visualization, Y.W. and J.B.; supervision, Y.Q. and J.B.; project administration, Y.Q. and J.L.; funding acquisition, Y.Q. and J.L. All authors have read and agreed to the published version of the manuscript.

**Funding:** The authors gratefully acknowledge the financial support of the Natural Science Basic Research Program of Shaanxi (Program No. 2023-JC-YB-328) and the financial support of the Fundamental Research Funds for the Central Universities (Program No. ZYTS23014).

**Data Availability Statement:** The raw data supporting the conclusions of this article will be made available by the authors on request.

**Conflicts of Interest:** The authors declare no conflicts of interest.

## Appendix A. Experimental Results for S45C Steel [44]

| Loading Paths | Phase Angle (°) | $\frac{\Delta\gamma}{2}$ | $\frac{\Delta\varepsilon}{2}$ | $\frac{\Delta\tau}{2}$ (MPa) | $\frac{\Delta\sigma}{2}$ (MPa) | $N_f$ (Cycles) |
|---|---|---|---|---|---|---|
| a | - | 0 | 0.025 | 0 | 595.19 | 110 |
| a | - | 0 | 0.01 | 0 | 480.15 | 852 |
| a | - | 0 | 0.005 | 0 | 389.1 | 3383 |
| a | - | 0 | 0.004 | 0 | 361.9 | 5514 |
| a | - | 0 | 0.015 | 0 | 509.02 | 421 |
| a | - | 0 | 0.004 | 0 | 365.46 | 8933 |
| a | - | 0 | 0.003 | 0 | 325.9 | 22071 |
| **a** | **-** | **0** | **0.015** | **0** | **500.16** | **407** |
| **b** | **-** | **0.015** | **0** | **287.14** | **0** | **1151** |
| b | - | 0.015 | 0 | 283.81 | 0 | 1761 |
| b | - | 0.015 | 0 | 286.3 | 0 | 1771 |
| b | - | 0.009 | 0 | 244.25 | 0 | 5644 |
| b | - | 0.008 | 0 | 229.38 | 0 | 14930 |
| **c** | **0** | **0.0052** | **0.006** | **103.55** | **370.33** | **2278** |
| c | 0 | 0.0082 | 0.009 | 111.4 | 395.16 | 568 |
| c | 0 | 0.0065 | 0.0072 | 108.88 | 391.11 | 1366 |
| **c** | **0** | **0.0065** | **0.0036** | **164.4** | **285.14** | **4647** |
| c | 0 | 0.0041 | 0.009 | 57.28 | 430.58 | 1181 |

| Loading Paths | Phase Angle (°) | $\frac{\Delta\gamma}{2}$ | $\frac{\Delta\varepsilon}{2}$ | $\frac{\Delta\tau}{2}$ (MPa) | $\frac{\Delta\sigma}{2}$ (MPa) | $N_f$ (Cycles) |
|---|---|---|---|---|---|---|
| d | 22.5 | 0.0082 | 0.018 | 184.9 | 554.4 | 215 |
| e | 45 | 0.0055 | 0.006 | 214.82 | 419.13 | 1631 |
| e | 45 | 0.0082 | 0.018 | 189 | 542.51 | 191 |
| f | 90 | 0.0041 | 0.009 | 156.27 | 456.77 | 678 |
| f | 90 | 0.0055 | 0.006 | 204.27 | 432.96 | 1617 |
| **f** | **90** | **0.0066** | **0.0077** | **267.5** | **514.23** | **435** |

## Appendix B. Experimental Results for 7075-T651 Aluminum Alloy [45]

| Loading Paths | Phase Angle (°) | $\frac{\Delta\tau}{2}$ (MPa) | $\frac{\Delta\sigma}{2}$ (MPa) | $\tau_m$ (MPa) | $\sigma_m$ (MPa) | $N_f$ (Cycles) |
|---|---|---|---|---|---|---|
| a | - | 0 | 315 | 0 | 0 | 35,094 |
| a | - | 0 | 260 | 0 | 0 | 181,817 |
| **a** | **-** | **0** | **260** | **0** | **0** | **159,980** |
| a | - | 0 | 235 | 0 | 0 | 848,760 |
| a | - | 0 | 215 | 0 | 0 | 1,187,357 |
| g | - | 0 | 203.04 | 0 | 228.95 | 87,622 |
| g | - | 0 | 183.54 | 0 | 206.96 | 198,247 |
| g | - | 0 | 183.3 | 0 | 206.69 | 175,509 |
| g | - | 0 | 183.3 | 0 | 206.69 | 139,329 |
| g | - | 0 | 183.3 | 0 | 206.69 | 391,636 |
| g | - | 0 | 181.42 | 0 | 204.56 | 660,226 |
| g | - | 0 | 178.6 | 0 | 201.38 | 373,265 |
| **g** | **-** | **0** | **169.2** | **0** | **190.79** | **1,134,075** |
| h | - | 105.83 | 0 | 119.34 | 0 | 730,491 |
| h | - | 117.16 | 0 | 132.11 | 0 | 243,363 |
| b | - | 117 | 0 | 0 | 0 | 2,159,208 |
| b | - | 117 | 0 | 0 | 0 | 1,217,964 |
| h | - | 151.33 | 0 | 170.64 | 0 | 19,500 |
| **h** | **-** | **151.33** | **0** | **170.64** | **0** | **46,893** |
| b | - | 151.33 | 0 | 0 | 0 | 207,445 |
| b | - | 151.33 | 0 | 0 | 0 | 187,227 |
| h | - | 139.12 | 0 | 156.88 | 0 | 209,904 |
| h | - | 134.24 | 0 | 151.38 | 0 | 210,668 |
| **h** | **-** | **134.24** | **0** | **151.38** | **0** | **310,472** |
| h | - | 134.24 | 0 | 151.38 | 0 | 246,343 |
| b | - | 134.24 | 0 | 0 | 0 | 1,179,056 |
| b | - | 180 | 0 | 0 | 0 | 56,421 |
| b | - | 210 | 0 | 0 | 0 | 13,630 |
| b | - | 210 | 0 | 0 | 0 | 23,898 |
| i | 0 | 83.47 | 144.57 | 94.12 | 163.02 | 65,046 |
| **i** | **0** | **83.47** | **144.57** | **94.12** | **163.02** | **53,058** |
| i | 0 | 75.02 | 129.94 | 84.6 | 146.53 | 270,597 |
| **i** | **0** | **75.02** | **129.94** | **84.6** | **146.53** | **126,438** |
| j | 30 | 79.63 | 137.92 | 89.79 | 155.53 | 178,920 |
| j | 30 | 75.02 | 129.94 | 84.6 | 146.53 | 747,389 |
| j | 30 | 88.26 | 152.87 | 99.53 | 172.39 | 36,299 |
| **j** | **30** | **88.26** | **152.87** | **99.53** | **172.39** | **37,525** |
| j | 30 | 83.47 | 144.57 | 94.12 | 163.02 | 64,231 |
| j | 30 | 83.47 | 144.57 | 94.12 | 163.02 | 82,445 |
| k | 45 | 75.02 | 129.94 | 84.6 | 146.53 | 934,710 |
| **k** | **45** | **75.02** | **129.94** | **84.6** | **146.53** | **1,527,482** |
| k | 45 | 79.63 | 137.92 | 89.79 | 155.53 | 89,852 |
| k | 45 | 83.47 | 144.57 | 94.12 | 163.02 | 167,161 |
| k | 45 | 83.47 | 144.57 | 94.12 | 163.02 | 56,775 |
| k | 45 | 85.39 | 147.89 | 96.29 | 166.77 | 105,315 |
| l | 90 | 83.47 | 144.57 | 94.12 | 163.02 | 94,718 |
| **l** | **90** | **83.47** | **144.57** | **94.12** | **163.02** | **70,333** |
| l | 90 | 88.26 | 152.87 | 99.53 | 172.39 | 51,324 |
| **l** | **90** | **88.26** | **152.87** | **99.53** | **172.39** | **68,455** |
| l | 90 | 88.26 | 152.87 | 99.53 | 172.39 | 147180 |
| m | 180 | 83.47 | 144.57 | 94.12 | 163.02 | 78,147 |
| m | 180 | 81.55 | 141.25 | 91.96 | 159.28 | 102,512 |

## References


1. Yang, J.Y.; Kang, G.Z.; Kan, Q.H. A novel deep learning approach of multiaxial fatigue life-prediction with a self-attention mechanism characterizing the effects of loading history and varying temperature. *Int. J. Fatigue* **2022**, *162*, 106851. [CrossRef]
2. Ngeru, T.; Kurtulan, D.; Karkar, A.; Hanke, S. Mechanical behaviour and failure mode of high interstitially alloyed austenite under combined compression and cyclic torsion. *Metals* **2022**, *12*, 157. [CrossRef]
3. Carpinteri, A.; Spagnoli, A.; Vantadori, S. A review of multiaxial fatigue criteria for random variable amplitude loads. *Fatigue Fract. Eng. Mater. Struct.* **2017**, *40*, 1007–1036. [CrossRef]
4. Luo, P.; Yao, W.; Susmel, L. An improved critical plane and cycle counting method to assess damage under variable amplitude multiaxial fatigue loading. *Fatigue Fract. Eng. Mater. Struct.* **2020**, *43*, 2024–2039. [CrossRef]
5. Yu, Z.Y.; Zhu, S.P.; Liu, Q.; Liu, Y.H. A new energy-critical plane damage parameter for multiaxial fatigue life prediction of turbine blades. *Materials* **2017**, *10*, 513. [CrossRef] [PubMed]
6. Kamal, M.; Rahman, M.M. Advances in fatigue life modeling: A review. *Renew. Sust. Energ. Rev.* **2018**, *82*, 940–949. [CrossRef]
7. Li, J.; Zhang, Z.P.; Sun, Q.; Li, C.W. Multiaxial fatigue life prediction for various metallic materials based on the critical plane approach. *Int. J. Fatigue* **2011**, *33*, 90–101. [CrossRef]
8. Zhou, J.; Huang, H.Z.; Li, H. A novel energy-critical multiaxial fatigue life prediction for low cycle fatigue under mixed-mode loading. *Metals* **2018**, *8*, 1066. [CrossRef]
9. Gao, S.L.; Yue, X.Z.; Wang, H. Predictability of different machine learning approaches on the fatigue life of additive-manufactured porous titanium structure. *Metals* **2024**, *14*, 320. [CrossRef]
10. Li, X.; Yang, H.R.; Yang, J.W. Fretting fatigue life prediction for aluminum alloy based on particle-swarm-optimized back propagation neural network. *Metals* **2024**, *14*, 381. [CrossRef]
11. Yang, J.Y.; Kang, G.Z.; Liu, Y.J.; Kan, Q.H. A novel method of multiaxial fatigue life prediction based on deep learning. *Int. J. Fatigue* **2021**, *151*, 106356. [CrossRef]
12. Smith, K.N.; Watson, P.; Topper, T.H. A stress-strain function for the fatigue of metals. *J. Mater.* **1970**, *5*, 767–778.
13. Kandil, F.A.; Brown, M.W.; Miller, K.J. Biaxial low-cycle fatigue failure of 316 stainless steel at elevated temperatures. In *Mechanical Behaviour and Nuclear Applications of Stainless Steel at Elevated Temperatures*; Metals Society: London, UK, 1982.
14. Fatemi, A.; Kurath, P. Multiaxial fatigue fife predictions under the influence of mean-stresses. *J. Eng. Mater. Technol.* **1988**, *110*, 380–388. [CrossRef]
15. Shang, D.G.; Wang, D.J. A new multiaxial fatigue damage model based on the critical plane approach. *Int. J. Fatigue* **1998**, *20*, 241–245.
16. Liu, T.Q.; Shi, X.H.; Zhang, J.Y.; Fei, B.J. Multiaxial high-cycle fatigue failure of 30CrMnSiA steel with mean tension stress and mean shear stress. *Int. J. Fatigue* **2019**, *129*, 105219. [CrossRef]
17. Chen, J.; Liu, Y.M. Fatigue modeling using neural networks: A comprehensive review. *Fatigue Fract. Eng. Mater. Struct.* **2022**, *45*, 945–979. [CrossRef]
18. Sun, X.Y.; Zhou, T.G.; Song, K.; Chen, X. An image recognition based multiaxial low-cycle fatigue life prediction method with CNN model. *Int. J. Fatigue* **2023**, *167*, 107324. [CrossRef]
19. Zhang, X.C.; Gong, J.G.; Xuan, F.Z. A deep learning based life prediction method for components under creep, fatigue and creep-fatigue conditions. *Int. J. Fatigue* **2021**, *148*, 106236. [CrossRef]
20. Feng, S.Z.; Xu, Y.; Han, X.; Li, Z.X.; Incecik, A. A phase field and deep-learning based approach for accurate prediction of structural residual useful life. *Comput. Methods Appl. Mech. Eng.* **2021**, *383*, 113885. [CrossRef]
21. Li, J.; Qiu, Y.Y. A path-dependent multiaxial fatigue life estimation criterion for metals under various loading conditions. *Int. J. Fatigue* **2021**, *149*, 106300. [CrossRef]
22. Zhu, P.N.; Gao, J.X.; Yuan, Y.P.; Wu, Z.F.; Xu, R.X. An improved multiaxial low-cycle fatigue life prediction model based on equivalent strain approach. *Metals* **2023**, *13*, 629. [CrossRef]
23. Kanazawa, K.; Miller, K.J.; Brown, M.W. Low-cycle fatigue under out-of-phase loading conditions. *J. Eng. Mater. Technol.* **1977**, *99*, 222–228. [CrossRef]
24. Ge, J.R.; Sun, Y.; Xu, J.; Yang, Z.Q.; Liang, J. Fatigue life prediction of metal structures subjected to combined thermal-acoustic loadings using a new critical plane model. *Int. J. Fatigue* **2017**, *96*, 89–101. [CrossRef]
25. Li, J.; Wang, X.; Li, K.; Qiu, Y.Y. A modification of Matake criterion for considering the effect of mean shear stress under high cycle fatigue loading. *Fatigue Fract. Eng. Mater. Struct.* **2021**, *44*, 1760–1782. [CrossRef]
26. Li, J.; Wang, X.; Li, R.T.; Qiu, Y.Y. Multiaxial fatigue life prediction for metals by means of an improved strain energy density-based critical plane criterion. *Eur. J. Mech. A-Solid.* **2021**, *90*, 104353. [CrossRef]
27. Johnston, E.R.J.; DeWolf, J.T.; Beer, F.P. *Mechanics of Materials*; McGraw-Hill: New York, NY, USA, 2001.
28. Fatemi, A.; Socie, D.F. A critical plane approach to multiaxial fatigue damage including out-of-phase loading. *Fatigue Fract. Eng. Mater. Struct.* **1988**, *11*, 149–165. [CrossRef]
29. Brown, M.W.; Miller, K.J. High temperature low cycle biaxial fatigue of two steels. *Fatigue Fract. Eng. Mater. Struct.* **1979**, *1*, 217–229. [CrossRef]
30. Pascoe, K.J.; Devilliers, J.W.R. Low cycle fatigue of steels under biaxial straining. *J. Strain Anal.* **1967**, *2*, 117–126. [CrossRef]
31. Socie, D.; Marquis, G. *Multiaxial Fatigue*; SAE International: Warrendale, PA, USA, 1999.

32. Zhang, W.; Akid, R. Effect of biaxial mean stress on cyclic stress-strain response and behaviour of short fatigue cracks in a high strength spring steel. *Fatigue Fract. Eng. Mater. Struct.* **1997**, *20*, 167–177. [CrossRef]
33. Portugal, I.; Olave, M.; Urresti, I.; Zurutuza, A.; López, A.; Muñiz-Calvente, M.; Fernández-Canteli, A. A comparative analysis of multiaxial fatigue models under random loading. *Eng. Struct.* **2019**, *182*, 112–122. [CrossRef]
34. Ince, A.; Glinka, G. A generalized fatigue damage parameter for multiaxial fatigue life prediction under proportional and non-proportional loadings. *Int. J. Fatigue* **2014**, *62*, 34–41. [CrossRef]
35. Wu, Z.R.; Li, X.; Fang, L.; Song, Y.D. Evaluation of multiaxial fatigue life prediction criteria for Ni-based superalloy GH4169. *Proc. Inst. Mech. Eng. Part C-J. Mech. Eng. Sci.* **2017**, *232*, 1823–1837. [CrossRef]
36. Wang, C.H.; Brown, M.W. A path-independent parameter for fatigue under proportional and non-proportional loading. *Fatigue Fract. Eng. Mater. Struct.* **1993**, *16*, 1285–1297. [CrossRef]
37. Wang, Y.J.; Zhu, Z.Y.; Sha, A.X.; Hao, W.F. Low cycle fatigue life prediction of titanium alloy using genetic algorithm-optimized BP artificial neural network. *Int. J. Fatigue* **2023**, *172*, 107609. [CrossRef]
38. Wang, C.Z.; Wang, Y.C.; Ye, Z.W.; Yan, L.Y.; Cai, W.C.; Pan, S. Credit card fraud detection based on whale algorithm optimized BP neural network. In Proceedings of the 2018 13th International Conference on Computer Science & Education (ICCSE), Colombo, Sri Lanka, 8–11 August 2018; pp. 1–4.
39. Li, Y.W.; Cao, K. Establishment and application of intelligent city building information model based on BP neural network model. *Comput. Commun.* **2020**, *153*, 382–389. [CrossRef]
40. Fan, J.L.; Zhu, G.L.; Zhu, M.L.; Xuan, F.Z. A data-physics integrated approach to life prediction in very high cycle fatigue regime. *Int. J. Fatigue* **2023**, *176*, 107917. [CrossRef]
41. Ma, X.Y.; Ma, X.J.; Wang, Z.L.; Song, S.L.; Sheng, Y.P. Investigation of changing SARA and fatigue properties of asphalt bitumen under ageing and analysis of their relation based upon the BP neural network. *Constr. Build. Mater.* **2023**, *394*, 132163. [CrossRef]
42. Shang, D.G.; Sun, G.Q.; Deng, J.; Yan, C.L. Multiaxial fatigue damage parameter and life prediction for medium-carbon steel based on the critical plane approach. *Int. J. Fatigue* **2007**, *29*, 2200–2207. [CrossRef]
43. Mu, C.; Qiu, B.Z.; Liu, X.H. A new method for figuring the number of hidden layer nodes in BP algorithm. *Int. J. Recent Innov. Trends Comput. Commun.* **2017**, *5*, 101–114.
44. Kim, K.S.; Park, J.C.; Lee, J.W. Multiaxial fatigue under variable amplitude loads. *J. Eng. Mater. Technol.* **1999**, *121*, 286–293. [CrossRef]
45. Wang, X.W.; Shang, D.G.; Sun, Y.J.; Chen, H. Multiaxial high-cycle fatigue life prediction model considering mean shear stress effect under constant and variable amplitude loading. *Theor. Appl. Fract. Mech.* **2018**, *96*, 676–687. [CrossRef]
46. Wu, S.D.; Shang, D.G.; Liu, P.C.; Hao, G.C.; Hou, G.; Shi, F.T.; Miao, B. Fatigue life prediction based on modified narrowband method under broadband random vibration loading. *Int. J. Fatigue* **2022**, *159*, 106832. [CrossRef]
47. Kim, K.S.; Chen, X.; Han, C.; Lee, H.W. Estimation methods for fatigue properties of steels under axial and torsional Loading. *Int. J. Fatigue* **2002**, *23*, 783–793. [CrossRef]
48. Gates, N.R.; Fatemi, A. On the consideration of normal and shear stress interaction in multiaxial fatigue damage analysis. *Int. J. Fatigue* **2017**, *100*, 322–336. [CrossRef]
49. Meggiolaro, M.A.; Castro, J.T.P. Statistical evaluation of strain-life fatigue crack initiation predictions. *Int. J. Fatigue* **2004**, *26*, 463–476. [CrossRef]
50. Socie, D.F. Multiaxial fatigue damage models. *J. Eng. Mater. Technol.* **1987**, *109*, 293–298. [CrossRef]
51. Shang, D.G.; Wang, D.J.; Xu, H.; Ping, A. A unified multiaxial fatigue damage parameter. *Acta. Mech. Solida. Sin.* **1998**, *11*, 261–274.
52. Wang, Y.T.; Qiu, Y.Y.; Li, J.; Bai, J. A hybrid frequency-time domain life prediction method based on the critical plane theory. *Fatigue Fract. Eng. Mater. Struct.* **2024**, *47*, 2351–2368. [CrossRef]